Journal of Applied Remote Sensing

RemoteSensing.SPIEDigitalLibrary.org

Object-based change detection method using refined Markov random field

Daifeng Peng
Yongjun Zhang

SPIE.

Daifeng Peng, Yongjun Zhang, "Object-based change detection method using refined Markov random field," *J. Appl. Remote Sens.* **11**(1), 016024 (2017), doi: 10.1117/1.JRS.11.016024.

Object-based change detection method using refined Markov random field

Daifeng Peng and Yongjun Zhang*
Wuhan University, School of Remote Sensing and Information Engineering, Wuhan, China

Abstract. In order to fully consider the local spatial constraints between neighboring objects in object-based change detection (OBCD), an OBCD approach is presented by introducing a refined Markov random field (MRF). First, two periods of images are stacked and segmented to produce image objects. Second, object spectral and textual histogram features are extracted and G-statistic is implemented to measure the distance among different histogram distributions. Meanwhile, object heterogeneity is calculated by combining spectral and textual histogram distance using adaptive weight. Third, an expectation-maximization algorithm is applied for determining the change category of each object and the initial change map is then generated. Finally, a refined change map is produced by employing the proposed refined object-based MRF method. Three experiments were conducted and compared with some state-of-the-art unsupervised OBCD methods to evaluate the effectiveness of the proposed method. Experimental results demonstrate that the proposed method obtains the highest accuracy among the methods used in this paper, which confirms its validness and effectiveness in OBCD. © *2017 Society of Photo-Optical Instrumentation Engineers (SPIE)* [DOI: 10.1117/1.JRS.11.016024]

Keywords: change detection; segmentation; spatial constraints; expectation-maximization; Markov random field.

Paper 16702 received Sep. 20, 2016; accepted for publication Jan. 19, 2017; published online Feb. 7, 2017.

1 Introduction

Remote sensing imagery is widely used in the research of change detection (CD) for the advantages of large coverage areas, short revisit time as well as abundant image information. CD is of great significance in the field of land use and land cover investigation, resource survey, urban expansion monitoring, environment assessment, and rapid response to disaster events.[1–4]

In the past decades, numerous CD methods have been proposed, and the investigations can mainly be divided into pixel-based and object-based methods.[5] In the first case, the change features from two images are compared for each pixel independently. In the second case, the images are segmented into disjoint and homogeneous objects, and then change features are extracted and compared for the objects. Pixel-based CD methods are mainly employed in medium- and low-resolution remote sensing imagery. Many pixel-based CD techniques have been developed, including postclassification comparison,[6] change vector analysis,[7] level set method,[8] kernel-based, and support vector machine method.[9]

With the ever-increasing availability of high-resolution images, object-based change detection (OBCD) has become increasingly popular for its great advantages over pixel-based CD. In OBCD, it is easy to model contextual information by analyzing spatial relationships and arrangements of image objects, and CD accuracy is less sensitive to the noises caused by radiometric calibration and image registration.[10,11] Generally, two main OBCD strategies can be categorized. The first strategy is carried out by object feature similarity analysis, where object features are extracted and feature vectors are constructed first, and change map is then generated by similarity analysis of feature vectors.[12–14] The second strategy is employed by class labels comparison,

*Address all correspondence to: Yongjun Zhang, E-mail: zhangyj@whu.edu.cn

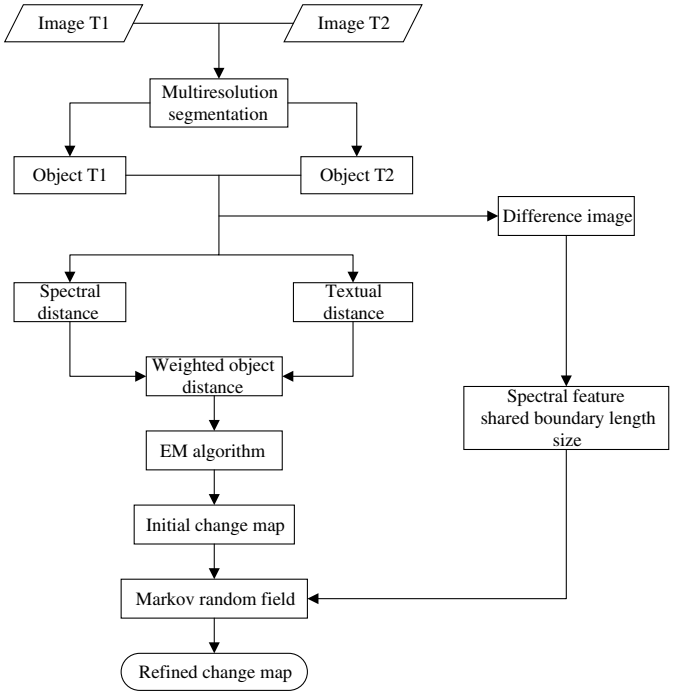

Fig. 1 Flow chart of the proposed CD method.

where image classification is implemented using object features, and change map is then generated by the comparison and analysis of the class membership.[15–17]

However, within the above OBCD methods, all objects are treated independently as a whole. In addition to that, due to the limitation of segmentation, different objects cannot be separated well and may suffer from spatial interactions to each other. To tackle these limitations, this paper presents an OBCD method by combining object-based expectation-maximization (OEM) and refined Markov random field (RMRF) model (OEM-RMRF), where local spatial constraints between neighboring objects can be considered well. The proposed approach mainly consists of four steps, as shown in Fig. 1. First, two periods of images are stacked as one image with double bands, and image objects are generated using watershed segmentation method. Second, object spectral and textual features are extracted by employing spectral and textual histograms, and G-statistic is implemented to measure the distance between different histogram distributions. Meanwhile, object heterogeneity is calculated by combining spectral and textual histogram distance with adaptive weight. Third, an EM algorithm is applied for determining the change category of each object and initial change map is then generated. Finally, a refined MRF model is constructed by utilizing object spectral, shape and size features, and the refined change map is then generated by applying the refined MRF model.

2 Proposed Change Detection Method

Considering two multispectral images X_1 and X_2 of size $M \times N$ with B bands acquired over the same geographical area at two different times, suppose that such images have been well preprocessed, including radiometric calibration and coregistration. Let X_i^b $(i = 1, 2)$ be the values of $M \times N$ pixels in the b'th $(1 \leq b \leq B)$ band of X_i, the difference image X_D can be defined as

$$X_D = \sqrt{\sum_{b=1}^{B} (X_1^b - X_2^b)^2}. \tag{1}$$

2.1 *Object Features Extraction and Heterogeneity Calculation*

In OBCD, objects are generated by either image segmentation or vector-raster integration, where image segmentation is most used for the absence of corresponding vectors. In our study, two

periods of images are stacked as one image with $2 \times B$ bands, and then watershed segmentation is implemented to generate image objects.[18] To measure the similarity of two corresponding objects, both spectral and textual features are extracted to avoid the drawback of using single feature, where raw gray values are used to represent object spectral feature while object textual feature is delineated by combining local binary pattern (LBP) and local contrast (LC).[19] Histogram is the statistic of feature values within the object, which is a robust and effective feature description method. In this method, object spectral feature is computed using color histograms, while textual feature is calculated by utilizing the joint histograms of LBP and LC. Meanwhile, G-statistic,[20] which is a nonparametric statistical method and a modification of Kullback–Leibler distance, is utilized to measure the distance of two histograms.

Let L be the gray level, let $f_i^b (b = 1,2,\ldots,B)$ be the frequency of gray value i in the object on band b. Hence, the histogram distance on band b can be calculated as:

$$G^b = 2\left\{\sum_{t_1,t_2}\sum_{i=0}^{L-1} f_i^b In(f_i^b) - \sum_{i=0}^{L-1}\left(\sum_{t_1,t_2} f_i^b\right) In\left(\sum_{t_1,t_2} f_i^b\right) + 2In2\right\}. \tag{2}$$

Then, object heterogeneity can be calculated by combining spectral and textual histogram distance. Assuming G_s^b and G_t^b represent spectral heterogeneity and textual heterogeneity, respectively, the heterogeneity after the combination is defined as:

$$H^b = \omega_s G_s^b + \omega_t G_t^b, \tag{3}$$

where ω_s and ω_t represent spectral weight and textual weight, respectively, which satisfies the formula $\omega_s + \omega_t = 1$. In our test, ω_s and ω_t are calculated using the method proposed by Hu.[18] Moreover, image entropy of each band is calculated and band weight ω_b is defined as:

$$\omega_b = E(b) / \sum_{i=1}^{B} E(i), \tag{4}$$

$$E(b) = -\sum_{l=0}^{L} p(l)\log[p(l)], \tag{5}$$

where $E(b)$ represents the entropy value of band b, L denotes the gray level in band b, and $p(l)$ is the probability of gray l in band b.

After the calculation of spectral and texture weights and band weights, we get the final heterogeneity for each object, which is defined as follow:

$$H^b = \sum_{b=1}^{B} \omega_b(\omega_s G_s^b + \omega_t G_t^b). \tag{6}$$

2.2 *Generation of Initial Change Map*

All the values of object heterogeneity make up a set $H = \{h_1, h_2, \ldots h_i, \ldots, h_N\}$, N is the number of objects. h_i represents the heterogeneity of i'th object. Elements in the set H can be divided into two categories: changed class and unchanged class. The heterogeneity values of the changed class are large while the values of the unchanged class are small. In this paper, elements in the set H are assumed to be a Gaussian mixture distribution composed of two Gaussian components, which are defined as follows:

$$p(h_k) = p(\omega_c)p(h_k|\omega_c) + p(\omega_n)p(h_k|\omega_n) \qquad k = 1,2,\ldots,N, \tag{7}$$

$$p(h_k|\omega) = \frac{1}{\sqrt{2\pi}\delta_\omega} \exp\left[-\frac{(h_k - \mu_w)^2}{2\delta_\omega^2}\right] \qquad \omega \in \{\omega_c, \omega_n\}, \tag{8}$$

where ω_c and ω_n represent the class of changed object and unchanged object, respectively. $p(\omega_c)$ and $p(\omega_n)$ denote the proportions of changed objects and unchanged objects, and $p(\omega_c) + p(\omega_n) = 1$. μ_ω is the mean value of the object, δ_ω is the standard deviation of the object.

To estimate the parameters of Gaussian mixture distribution, EM algorithm is employed, which can effectively find local maximum likelihood value in the missing data.[21] Based on the estimates of Gaussian mixture distribution, Bayes discriminant rule is then applied to calculate the threshold for classifying the objects into "change" and "no-change," whereby initial change map is generated.[22]

2.3 *Constructing of the Refined MRF Model*

In order to introduce the MRF model, neighbor system and clique system of each object have to be defined first. In traditional pixel-based CD method using MRF, 4-neighborhood or 8-neighborhood is mostly utilized to incorporate spatial information.[22–24] However, this is not the case in OBCD for the number of neighboring objects varies dynamically. Assuming that only the neighboring objects influence the class property of the central object, we use the neighboring objects as the neighbor system, which is shown in Fig. 2.

Let O_i be the i'th object. As for O_5, four neighboring objects are available, namely O_1, O_2, O_3, O_4, and the corresponding clique system are β_1, β_2, β_3, β_4, which means that only the four objects are used when introducing MRF model for O_5.

Suppose the object difference image $X = \{x_{O_1}, x_{O_2}, x_{O_3}, \ldots, x_{O_n}\}$ is given, and $L = \{l_1, l_2, l_3, \ldots, l_c\}$ denotes the class label of the object difference image and c is the number of classes. Then, the maximum a posteriori is adopted to produce the labels of objects, and the formulation could be defined as:

$$\hat{L} = \text{argmax}\{P(X|L)P(L)\}, \tag{9}$$

where $\hat{L}$ is the true label for the image and $P(X|L)$ is the joint probability density function of the object feature values in the object difference image. $P(L)$ is a prior probability distribution of the class labels of the object difference image.

In terms of MRF approach, maximizing the posterior probability in Eq. (9) is equivalent to minimize the following energy function $U_{\text{MRF}}(x_{O_i})$ for each object x_{O_i}

$$U_{\text{MRF}}(x_{O_i}) = U_{\text{spectral}}(x_{O_i}) + U_{\text{spatial}}(x_{O_i}), \tag{10}$$

where $U_{\text{spectral}}(x_{O_i})$ describes the spectral energy function from the object difference image and $U_{\text{spatial}}(x_{O_i})$ represents the spatial energy term calculated from the local neighboring objects of object x_{O_i}.

A variety of studies have been carried out on difference image analysis in unsupervised CD, where a Gaussian mixture model is mostly applied to model the difference image effectively.[21,22,25,26] Based on this, we assume that the object feature values of the given class in the object difference image are independent to each other and supposed to be Gaussian distribution. Hence, the detailed spectral energy term can be written as:

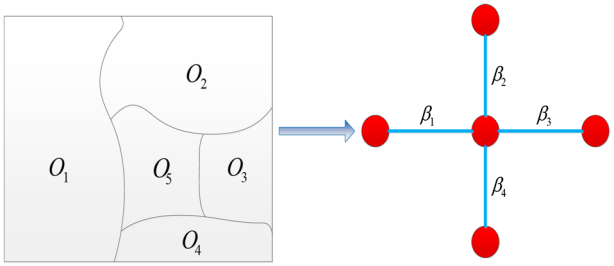

Fig. 2 An illustration of neighborhood and clique system.

$$U_{\text{spectral}}(x_{O_i}) = \frac{1}{2} In(2\pi|\Sigma_c|) + \frac{1}{2}(X_{O_i} - \mu_c)\Sigma_c^{-1}(X_{O_i} - \mu_c)^T, \tag{11}$$

where μ_c and Σ_c are the mean vector and covariance matrix of class c, respectively, which can be calculated from the initial change map generated by EM algorithm. Furthermore, the spatial energy of object x_{O_i} is defined as:

$$U_{\text{spatial}}(x_{O_i}) = \sum_{j \in N_i} I[l(x_{O_i}), l(x_{O_j})], \tag{12}$$

where N_i denotes the spatial neighboring objects of object x_{O_i}, $I(.,.)$ is the indicator function, which measures the influence of two neighboring objects, $l(x_{O_i})$ and $l(x_{O_j})$ represent the category labels of the object x_{O_i} and its neighboring object x_{O_j}, respectively. Then, a graph-cut algorithm is utilized to search for the optimal result of Eq. (10) to solve the minimum value of MRF energy function.[27]

Both spectral and spatial features are considered to measure the influence of two neighboring objects. For the object x_{O_i} and its neighboring object $x_{O_j}(j \in N_i)$, it is assumed that the influence of x_{O_j} on x_{O_i} will be larger if the spectral difference of two adjacent objects is smaller, the size of x_{O_j} is larger and the length of shared boundary is longer. Hence, the indication function can be defined as:

$$I[l(x_{O_i}), l(x_{O_j})] = \begin{cases} \frac{|\mu_{x_{O_i}} - \mu_{x_{O_j}}|}{L_b^{\lambda}} + \beta \frac{n_{O_j}}{n_{O_i} + n_{O_j}} & \text{if } l(x_{O_i}) \neq l(x_{O_j}) \\ \frac{|\mu_{x_{O_i}} - \mu_{x_{O_j}}|}{L_b^{\lambda}} - \beta \frac{n_{O_j}}{n_{O_i} + n_{O_j}} & \text{if } l(x_{O_i}) = l(x_{O_j}) \end{cases}, \tag{13}$$

where $\mu_{x_{O_i}}$ and $\mu_{x_{O_j}}$ are the mean value of object x_{O_i} and x_{O_j} in object difference image, respectively, L_b denotes the length of shared boundary, λ is defined as the spatial parameter to adjust the constraint of the shared boundary. β is the penalty coefficient defined manually, which tunes the influence of neighboring object x_{O_j} on x_{O_i}, n_{O_i} and n_{O_j} are the size of object x_{O_i} and x_{O_j}. By this way, the refined MRF model is introduced in OBCD, and the final CD map would fully consider the spatial attraction among neighboring objects.

3 Data Set Description and Experiments Design

3.1 *Description of Data Sets*

Three multitemporal remote-sensing image data sets were applied in the proposed method. The first dataset is made up of two SPOT5 multispectral images (2644×1938 pixels, 2.5 m per pixel), acquired over the region of Guangzhou (China) in November 2006 and again in November 2007. A section (877×738 pixels) of the two scenes was selected as the subset for the experiment, as shown in Figs. 3(a) and 3(b). The second data set refers to two SPOT5 multispectral images (2644×1938 pixels, 2.5 m per pixel) obtained over another region of Guangzhou (China) in each October of 2006 and 2007, separately. A subset (1239×923 pixels) of the entire scene was cropped as the test site, as shown in Figs. 4(a) and 4(b). The third data set denotes two GF-1 fusion images ($18{,}192 \times 17{,}999$ pixels, 2 m per pixel) acquired over the region of Huangyan (China) in November 2013 and January 2015, a subset (554×527 pixels) of the two scenes was clipped for the experiment, as shown in Figs. 5(a) and 5(b). All the datasets were automatically coregistered with the algorithm developed by Zhang et al.[28] The root mean square error of registration was less than 0.5 pixels. The relative radiometric correction was implemented by applying the pseudoinvariant feature method.[29]

For each testing data set, a reference change map was prepared for quantitative evaluation purposes, which was manually generated according to a detailed visual interpretation as shown in Figs. 3(c), 4(c), and 5(c). The white areas are the changed areas while the black areas are the unchanged.

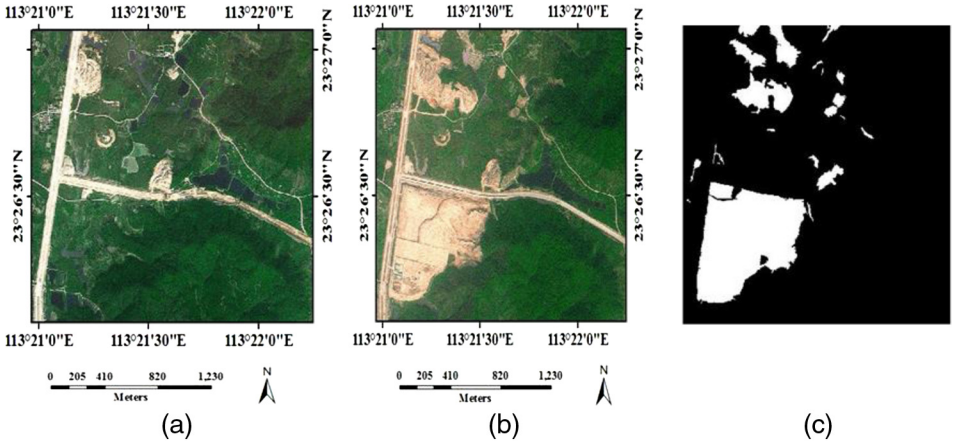

Fig. 3 Images in data set 1. (a) Image acquired in 2006, (b) image acquired in 2007, and (c) reference change map.

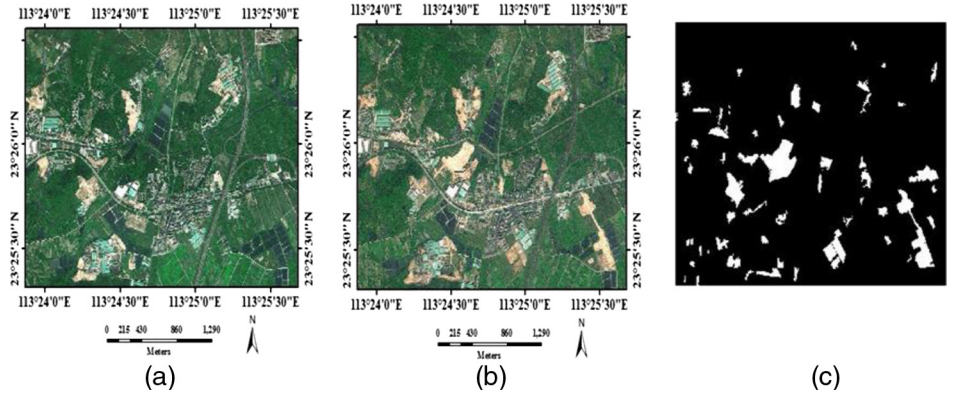

Fig. 4 Images in data set 2. (a) Image acquired in 2006, (b) image acquired in 2007, and (c) reference change map.

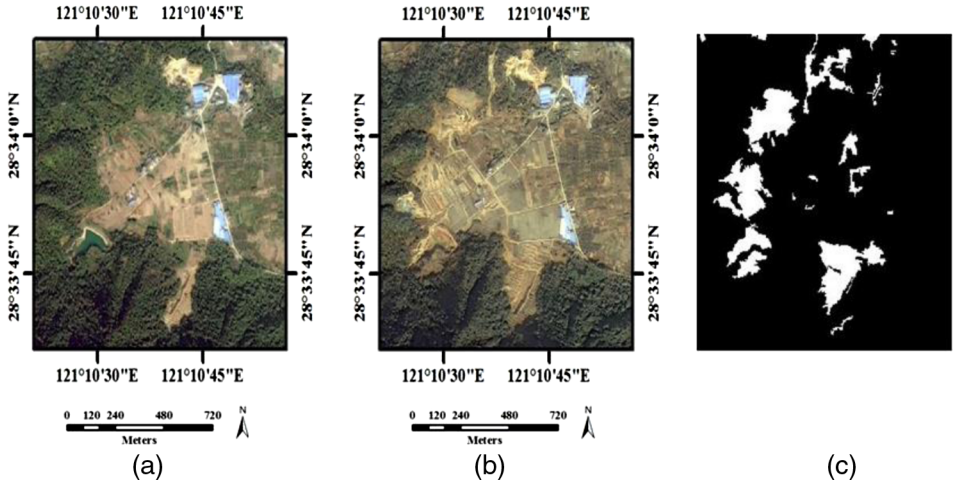

Fig. 5 Images in data set 3. (a) Image acquired in 2013, (b) image acquired in 2015, and (c) reference change map.

3.2 *Experiment Design*

The proposed OEM-RMRF method was compared to the OEM[21] and OEM-MRF (where original MRF model was used)[22] methods by experimenting on three multispectral remote sensing datasets to verify its effectiveness. The CD results are evaluated by four indexes: (1) false alarm

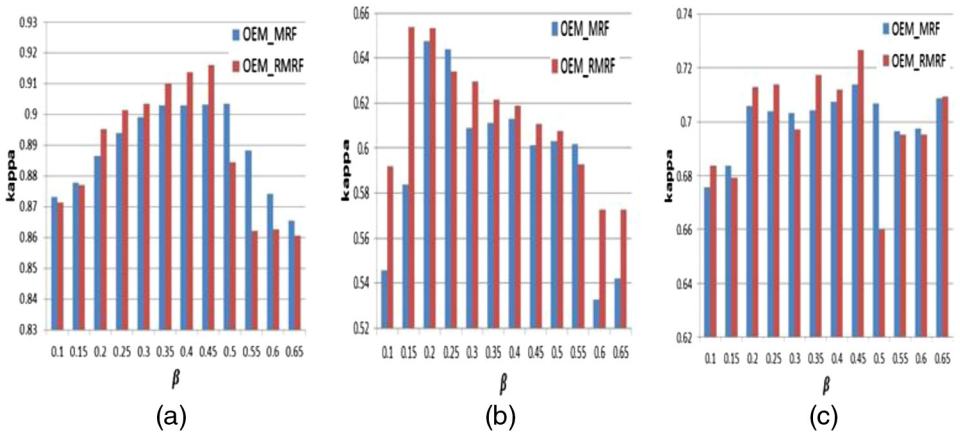

Fig. 6 Influence of different β values on the performance of OEM_MRF and OEM_RMRF method. (a) Kappa coefficient for data set 1. (b) Kappa coefficient for data set 2. (c) Kappa coefficient for data set 3.

rate (FA: number of unchanged pixels wrongly detected as changed pixels over the total number of unchanged pixels), (2) miss alarm rate (MA: number of changed pixels detected as unchanged pixels over the total number of changed pixels), (3) overall accuracy (OA: total number of rightly detected pixels over the total number of pixels), and (4) Kappa coefficient.[30]

3.3 *Parameter Setting for Experiments*

The smooth parameter β is of great importance when applying the MRF model. Noise pixels or objects could not be removed when β is set small, while oversmooth results will be caused when β is set large. In this section, a series of β values are set and the corresponding CD results are analyzed. Figure 6 shows the comparison of the performance of OEM_MRF and OEM_RMRF method in terms of different β. As can be seen from Fig. 6, kappa coefficient increase with the increase of β at first, while gradually decrease with the further increase of β after reaching a peak value. And the optimal β should be set at 0.45 in data set1 and data set 3, while it is set at 0.20 in data set 2. The maxi number of iterations of graph-cut algorithm in OEM_MRF and OEM_RMRF method is fixed as 10. The spatial constraint parameter λ is set at 0.5 as suggested by Hu.[18]

4 Experimental Results and Analysis

Figure 7 shows the experiment results carried out on data set 1. Due to the limitation of OBCD, many linear objects [e.g., region A and region B in Fig. 7(a)] are falsely detected as changed. Spatial constraints between neighboring objects are well considered in the MRF model, and the false alarms caused by linear objects can be well removed as can be seen in Figs. 7(b) and 7(c). Moreover, some false alarms [e.g., region C in Fig. 7(a)] due to the limitation of OEM can also be removed when introducing MRF model. All neighboring objects are treated with the same influence on the central objects in OEM_MRF, which is not the real case especially when the neighboring objects have shape and spectral difference. Compared with OEM_MRF, object spectral difference, size difference, and the length of shared boundary are taken into account to construct a refined MRF model in OEM_RMRF, whereby less false alarms arise and the CD accuracy is improved. The kappa coefficient of OEM_RMRF achieves the maximum of 0.92 as shown in Table 1, which verifies the effectiveness of our proposed method.

The visual results of different methods for data set 2 are shown in Fig. 8. We can see that there exist many falsely detected linear objects [e.g., regions A, B, C in Fig. 8(a)] with OEM method, which seriously affects the CD accuracy. And some false alarms [e.g., regions D, E in Fig. 8(a)] were caused due to the limitation of OEM still exist widely. When introducing the MRF model, the OBCD accuracy increases dramatically, where the FA falls sharply by 24.72% and 27.71%,

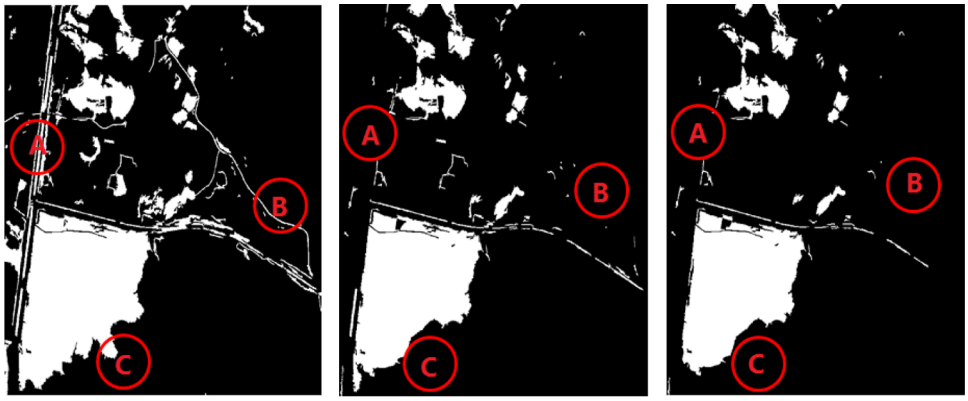

(a) (b) (c)

Fig. 7 CD results obtained using different methods for data set 1. (a) OEM. (b) OEM_MRF. (c) OEM_RMRF.

Table 1 Summary of the quantitative evaluations for OBCD methods on the three data sets.

Data set	Methods	FA (%)	MA (%)	OA (%)	Kappa
Data set 1	OEM	31.19	1.06	92.79	0.75
	OEM_MRF	8.84	1.34	97.53	0.90
	OEM_RMRF	**4.70**	**1.65**	**97.91**	**0.92**
Data set 2	OEM	46.17	1.99	91.50	0.51
	OEM_MRF	21.45	3.10	95.95	0.64
	OEM_RMRF	**18.46**	**3.53**	**96.28**	**0.65**
Data set 3	OEM	47.92	1.08	90.70	0.61
	OEM_MRF	19.28	3.47	95.68	0.71
	OEM_RMRF	**16.87**	**3.50**	**96.32**	**0.73**

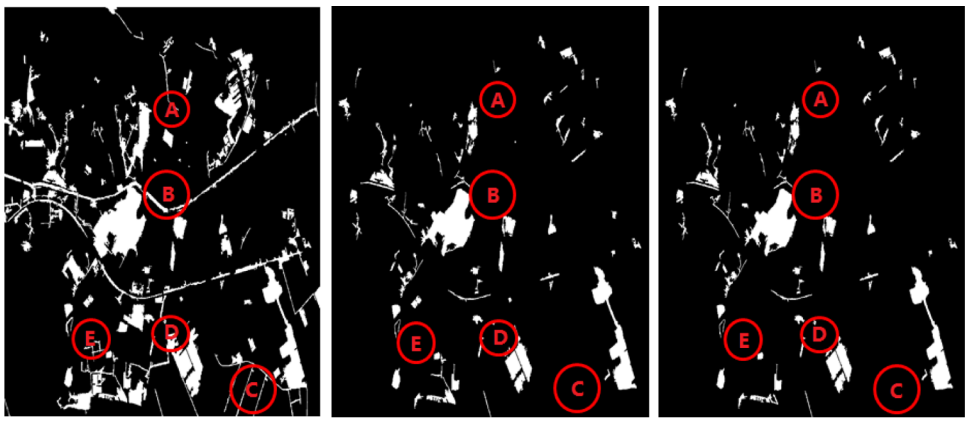

(a) (b) (c)

Fig. 8 CD results obtained using different methods for data set 2. (a) OEM. (b) OEM_MRF. (c) OEM_RMRF.

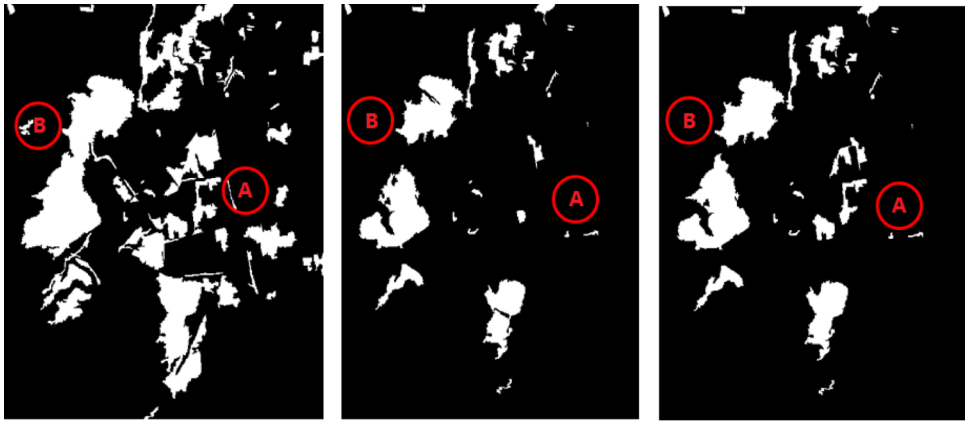

Fig. 9 CD results obtained using different methods for data set 3. (a) OEM. (b) OEM_MRF. (c) OEM_RMRF.

respectively, in the OEM_MRF and OEM_RMRF method, and the OA increases by 4.45% and 4.78%, respectively (as shown in Table 1), which indicates the effectiveness of increasing spatial constraints between neighboring objects in improving OBCD accuracy. Compared with OEM_MRF, OEM_RMRF further increases the OBCD accuracy by fully considering the spectral, shape, and size difference of the neighboring objects, where the OA increases by 0.33% and the kappa coefficient increases by 0.01 (as seen in Table 1).

Figure 9 shows the experimental results of different methods carried out for data set 3. We can see that false alarms caused by linear objects [e.g., region A in Fig. 9(a)] and the limitation of OEM [e.g., region B in Fig. 9(a)] still exist. And the false alarms can be removed when incorporating MRF model, as shown in Figs. 9(b) and 9(c). Compared with OEM, OEM_MRF increases the kappa coefficient by 0.1, and the kappa coefficient of our proposed method achieves the maximum of 0.73 (as seen from Table 1), which verifies the effectiveness of the proposed refined MRF model.

On average, we can see in Table 1 that FA can be reduced by 20% and OA can be increased by 5% when introducing MRF model in the three data sets. Meanwhile, our proposed OEM_RMRF method can further improve the performance of OBCD for the more accurate definition of neighboring object influence, which verifies its effectiveness in utilizing the spatial constraints.

5 Conclusion

In this paper, a refined MRF model was integrated with an EM algorithm for OBCD, which avoided the drawback of treating each object independently in traditional OBCD. Object spectral, shape, and size difference were fully considered when constructing the refined MRF model, which was more accurate than traditional MRF model. Three experiments were conducted to assess the performance of the proposed OEM_RMRF method. Through the comparison and analysis with OEM and OEM_MRF, we could draw the conclusion that spatial constraints are of great importance in OBCD, the OBCD accuracy could be improved greatly by introducing MRF model. Moreover, the proposed OEM_RMRF could further improve OBCD accuracy for the interactions between neighboring objects are more accurately delineated. Therefore, it is well confirmed that the proposed OEM_RMRF is an effective approach for OBCD.

Acknowledgments

This work was supported in part by the National Natural Science Foundation of China under Grant Nos. 41571434 and 41322010.

References

1. P. Coppin et al., "Digital change detection methods in ecosystem monitoring: a review," *Int. J. Remote Sens.* **25**(9), 1565–1596 (2004).
2. N. B. Chang et al., "Change detection of land use and land cover in an urban region with SPOT-5 images and partial Lanczos extreme learning machine," *J. Appl. Remote Sens.* **4**(1), 043551 (2010).
3. T. Ahmed, D. Singh, and R. Balasubramanian, "Potential application of Kanade-Lucas-Tomasi tracker on satellite images for automatic change detection," *J. Appl. Remote Sens.* **10**(2), 026018 (2016).
4. J. Shermeyer and B. Haack, "Remote sensing change detection methods to track deforestation and growth in threatened rainforests in Madre de Dios, Peru," *J. Appl. Remote Sens.* **9**(1), 096040 (2015).
5. K. Nackaerts et al., "Comparative performance of a modified change vector analysis in forest change detection," *Int. J. Remote Sens.* **26**(5), 839–852 (2005).
6. S. Ghosh, M. Roy, and A. Ghosh, "Semi-supervised change detection using modified self-organizing feature map neural network," *Appl. Soft Comput.* **15**(3–4), 1–20 (2014).
7. L. Bruzzone and D. F. Prieto, "Automatic analysis of the difference image for unsupervised change detection," *IEEE Trans. Geosci. Remote Sens.* **38**(3), 1171–1182 (2000).
8. G. Cao, "Automatic change detection in remote sensing images using level set method with neighborhood constraints," *J. Appl. Remote Sens.* **8**(1), 083678 (2014).
9. R. Shah-Hosseini, S. Homayouni, and A. Safari, "Environmental monitoring based on automatic change detection from remotely sensed data: kernel-based approach," *J. Appl. Remote Sens.* **9**(1), 095992 (2015).
10. M. Hussain et al., "Change detection from remotely sensed images: from pixel-based to object-based approaches," *ISPRS J. Photogramm. Remote Sens.* **80**(2), 91–106 (2013).
11. A. P. Tewkesbury et al., "A critical synthesis of remotely sensed optical image change detection techniques," *Remote Sens. Environ.* **160**, 1–14 (2015).
12. S. Bontemps et al., "An object-based change detection method accounting for temporal dependences in time series with medium to coarse spatial resolution," *Remote Sens. Environ.* **112**(6), 3181–3191 (2008).
13. C. Wang et al., "Object-oriented change detection approach for high-resolution remote sensing images based on multiscale fusion," *J. Appl. Remote Sens.* **7**(1), 073696 (2013).
14. B. Wang et al., "Object-based change detection of very high resolution satellite imagery using the cross-sharpening of multi-temporal data," *IEEE Geosci. Remote Sens. Lett.* **12**(5), 1151–1155 (2015).
15. G. Xian and C. Homer, "Updating the 2001 national land cover database impervious surface products to 2006 using landsat imagery change detection methods," *Remote Sens. Environ.* **114**(8), 1676–1686 (2010).
16. Y. Yang et al., "An integrated spatio-temporal classification method for urban fringe change detection analysis," *Int. J. Remote Sens.* **33**(8), 2516–2531 (2012).
17. Y. Qin et al., "Object-based land cover change detection for cross-sensor images," *Int. J. Remote Sens.* **34**(19), 6723–6737 (2013).
18. Z. Hu et al., "A spatially-constrained color-texture model for hierarchical VHR image segmentation," *IEEE Geosci. Remote Sens. Lett.* **10**(1), 120–124 (2013).
19. T. Ojala and M. Pietikäinen, "Unsupervised texture segmentation using feature distributions," *Pattern Recognit.* **32**(3), 477–486 (1999).
20. T. Ojala, M. Pietikäinen, and T. Mäenpää, "Gray-scale and rotation invariant texture classification with local binary patterns," in *European Conf. on Computer Vision*, pp. 404–420, Springer-Verlag (2000).
21. L. Li et al., "Change detection based on similarity measurement of object histogram using high-resolution remote sensing imagery," *J. Remote Sens.* **18**(1), 139–153 (2014).
22. L. Bruzzone and D. F. Prieto, "Automatic analysis of the difference image for unsupervised change detection," *IEEE Trans. Geosci. Remote Sens.* **38**(3), 1171–1182 (2000).
23. M. Hao et al., "Unsupervised change detection using fuzzy c-means and MRF from remotely sensed images," *Remote Sens. Lett.* **4**(12), 1185–1194 (2013).

24. P. He et al., "Advanced Markov random field model based on local uncertainty for unsupervised change detection," *Remote Sens. Lett.* **6**(9), 667–676 (2015).
25. Y. Bazi, L. Bruzzone, and F. Melgani, "An unsupervised approach based on the generalized Gaussian model to automatic change detection in multitemporal SAR images," *IEEE Trans. Geosci. Remote Sens.* **43**(4), 874–887 (2005).
26. T. Celik and K. K. Ma, "Unsupervised change detection for satellite images using dual-tree complex wavelet transform," *IEEE Trans. Geosci. Remote Sens.* **48**(3), 1199–1210 (2010).
27. R. Szeliski et al., "A comparative study of energy minimization methods for Markov random fields with smoothness-based priors," *IEEE Trans. Pattern Anal. Mach. Intell.* **30**(6), 1068–1080 (2008).
28. J. Zhang et al., "A highly repeatable feature detector: improved Harris-Laplace," *Multimedia Tools Appl.* **52**(1), 175–186 (2011).
29. A. N. Bao et al., "Comparison of relative radiometric normalization methods using pseudo-invariant features for change detection studies in rural and urban landscapes," *J. Appl. Remote Sens.* **6**(10), 063578 (2012).
30. G. M. Foody, "Thematic map comparison: evaluating the statistical significance of differences in classification accuracy," *Photogramm. Eng. Remote Sens.* **70**(5), 627–633 (2004).

Daifeng Peng is a PhD candidate at the School of Remote Sensing and Information Engineering, Wuhan University, China. He received his MS degree in photogrammetry and remote sensing from Wuhan University in 2014. His current research interests are in the areas of remote sensing image processing and change detection.

Yongjun Zhang is a professor at the School of Remote Sensing and Information Engineering, Wuhan University. He received his MS and PhD degrees in geomatics at the School of Geodesy and Geomatics, Wuhan University, China, in 2000 and 2002, respectively. His research interests include space, aerial, and low altitude photogrammetry, image matching, combined bundle adjustment with multisource data sets, 3-D city reconstruction, and industrial inspection.